Regular Article

PHYSICAL CHEMISTRY RESEARCH
Published by the
Iranian Chemical Society
www.physchemres.org
info@physchemres.org

Phys. Chem. Res., Vol. 12, No. 2, 407-417, June 2024
DOI: 10.22036/pcr.2023.406282.2373

Structural, Optical, and Magnetic Studies of Palladium (Pd) Doped Cerium Oxide (CeO_2) Nano Particles

C. Kumaran[a], I. Baskaran[b,*], P. Rajkumar[c], S. Selvaraj[c,*] and G.P. Sheeja Mol[d]

[a]*Department of Physics, Sri Akilandeswari Women's College, Wandiwash, 604408, Tamil Nadu, India*

[b]*Department of Physics, Arignar Anna Government Arts College, Cheyyar, 604407, Tamil Nadu, India*

[c]*Department of Physics, Saveetha School of Engineering, Saveetha Institute of Medical and Technical Sciences (SIMATS), Thandalam, Chennai, 602105, Tamil Nadu, India*

[d]*PG Department of Physics, St. Joseph's College for Women, Alappuzha, 688001, Kerala, India, Affiliated to University of Kerala, Thiruvananthapuram, 695034, Kerala, India*

(Received 9 July 2023, Accepted 6 September 2023)

In this study, an innovative method is used in the synthesis of Pd-doped CeO_2 nanoparticles through co-precipitation, with a focus on an extensive characterization of their structural, optical, and magnetic properties. Powder X-ray diffraction (XRD) and scanning electron microscopy (SEM) confirm a cubic structure *via* XRD and spherical morphology through SEM, respectively. Energy-dispersive X-ray spectroscopy (EDAX) further corroborated the presence of Pd, Ce, and O constituents in these nanoparticles. An intriguing finding revolves around the optical band gap, as Pd concentration increased, the optical band gap diminished from 2.92 eV to 2.25 eV, spanning from $Pd_{0.00}Ce_{100}O_2$ to $Pd_{5.0}Ce_{95.0}O_2$. Chemical bonding analysis via X-ray Photoelectron Spectroscopy (XPS) confirmed the presence of Ce, O, and Pd elements with distinct binding energies: Ce 3d at 850-920 eV, O1s at 530 eV, and Pd 3d at 360 eV. Additionally, Raman spectra displayed a prominent peak at 464.01 cm^{-1}, indicating a slight deviation from the bulk CeO_2's typical Raman active mode at 459 cm^{-1}, hinting at potential phonon confinement effects due to reduced particle size. Besides, magnetic studies unveiled enhanced properties in 5% Pd-doped CeO_2, transitioning from diamagnetic to paramagnetic behaviour.

Keywords: Pd-doped CeO_2, XRD, SEM, XPS, EDAX, Raman

INTRODUCTION

Palladium (Pd) and Cerium (Ce), both rare earth elements, have interesting bioactive qualities that have drawn much attention from researchers. Metallic nanoparticles made from Pd and Ce have a lot of potential in many areas, such as medicine, biology, and energy. These metals are utilized as catalysts in the creation of prodrug activators, anticancer agents, photothermal agents, biomolecule transporters, and antibacterial and antitumor agents [1-6]. Additionally, Pd nanoparticles (NPs) and their composite's abilities to manage environmental contamination have drawn attention. However, due to their coating, which boosts therapeutic efficacy, polymer-based nanoparticles have drawn significant attention in nanotechnology and biomedicine. Conventional, pricey, and risky techniques like chemical reduction, precipitation, and electrochemical synthesis are used to create these nanomaterials.

The advantages of using polymeric NPs as medication delivery systems cover a wide range of benefits. These include their potential use in controlled drug release, their capacity to protect medications and other physiologically active substances from outside effects, their improved bioavailability, and their therapeutic potency [7]. The antibacterial, catalytic, and anticancer capabilities of

*Corresponding authors. E-mail: ibk1978@gmail.com; sselvaphy@gmail.com

nanoparticles made of metals such as copper (Cu), palladium (Pd), cerium oxide (CeO), silver (Ag), platinum (Pt), iron oxide (FeO), zinc oxide (ZnO), titanium dioxide (TiO_2), and bimetallic Pt-Pd nanoparticles have been recognized [8-10]. However, the therapeutic efficacy of these substances is limited due to issues related to instability and agglomeration [11].

Cerium Oxide (CeO_2) displays magnetic properties in a variety of ways depending on the different materials production processes for instance, bulk CeO_2 exhibits diamagnetic behaviour, but CeO_2 nanoparticles exhibit Para magnetism at room temperature. Additionally, in 0.5 and 1% Pd doped CeO_2 nanoparticles, Transition Metal (TM) and Rare Earth (RE) doped CeO_2 exhibit ferromagnetic behaviour at ambient temperature. However, the Face Centered Exchange (FCE) mechanism, which is the basis for explaining the formation of Room Temperature Ferromagnetic Material (RTFM) for thin films and CeO_2 nanoparticles, is still up for debate. Due to the magnetically ordered spin of 3D dopants or surface imperfections, both pure and doped CeO_2 samples exhibit magnetic properties. Nevertheless, only a limited number of discoveries exist that provide support for the FCE mechanism and double exchange interaction as explanations for the origin of RTFM in a Ni-doped polycrystalline CeO_2 sample [12-15]. In order to further understand the cause of RTFM in these samples, a systematic investigation of the CeO_2 samples doped with Pd-ions must be conducted under the current situation.

In this article, we've used a low-temperature solid-state reaction technique to synthesize $Pd_x Ce_{100-x}O_2$ with x equal to 0, 0.5, 1, 3, and 5 mole (%) samples. X-ray Diffraction (XRD), Ultra Violet-Visible (UV-Vis) optical absorption spectroscopy, vibrating sample magnetometer (VSM) and X-ray photoelectron spectroscopy (XPS) studies, scanning electron microscopy (SEM), Brunauer-Emmett-Teller (BET) and Beta Surface Area Analysis of Solid material (BETSSA) have all been used to investigate the structural optical, magnetic, and electronic structure properties of synthesized nanoparticles.

EXPERIMENT DETAILS

In a standard synthesis method, Pd $(NO_3)_2.6H_2O$ (50 mM) and $Ce(NO_3)_3.6H_2O$ were homogenously ground together, combined, and subsequently dissolved in 100 ml of distilled water while continuously stirring with a magnetic stirrer. To prevent polymerization, a measurable amount (4 ml) of polyethylene glycol (PEG) with a molecular weight of PEG at a concentration of 10% was added. Additionally, 10 ml (5%) of sodium hydroxide (NaOH) solution was introduced into the mixture to achieve a pH value of 11, followed by sonication for 30 min. The resulting solution was heated at 110 ºC for 24 h. The Pd substituted samples were prepared using different compositions denoted by the formula $Pd_x Ce_{100-x}O_2$, where x represents the mole (%) percentage range 0, 0.5, 1, 3, and 5. In order to obtain the final products, the solution was repeatedly washed and filtered with distilled water. The samples were then washed with anhydrous ethanol and dried at 100 °C in a vacuum environment. A schematic of the procedures required to produce Pd-doped CeO_2 nanoparticles is shown in Fig. 1. This diagram is meant to be used as a guide, as it illustrates the main steps of the synthesis process.

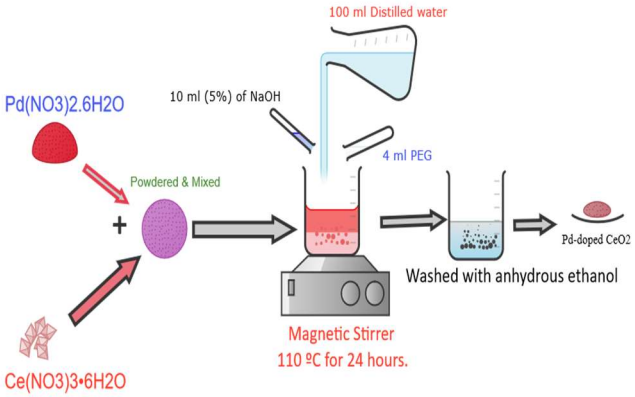

Fig. 1. Synthesis of Pd-doped CeO_2 nanoparticles.

RESULTS AND DISCUSSION

XRD Analysis of Pure and Pd-doped CeO_2: Phase Evolution and Peak Shifts

The indexed powder XRD patterns of $Pd_x Ce_{100-x}O_2$ with varying percentages of polycrystalline samples were depicted in Fig. 2. The Miller indices (111), (200), (220), (311), (222), (400), and (331) are employed to identify all seven Bragg peaks discovered in XRD patterns, which are analogous to

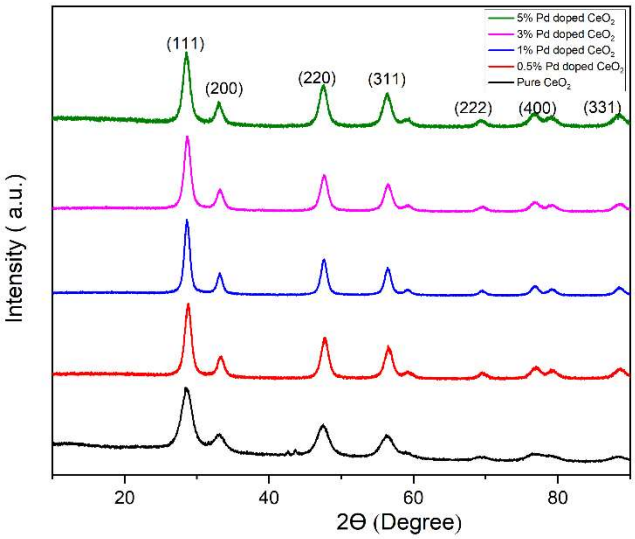

Fig. 2. XRD patterns of pure and Pd-doped CeO_2.

the structure of face-centered cubic fluorite found in of CeO_2. In Pd-doped CeO_2 samples, no unindexed peaks corresponding to secondary phases were observed, indicating the absence of such phases. This absence of secondary phases related to Pd-based impurities such as FeO, Co_2O_3, or Co_3O_4 verifies the single-phase development of $Pd_x Ce_{100-x}O_2$ with varying percentages in the samples.

In spite of this, the incorporation of palladium (Pd) doping has resulted in discernible shifts in the intensity peaks associated with CeO_2. In the case of 5% Pd-doped CeO_2, a higher intensity peak is evident, and the decreasing intensity of the peak indicates the movement of Ce ions to interstitial sites due to the substitution of Ce^{4+} ions by Pd^{2+} or Pd^{3+} ions, resulting in a lower concentration of the elements in these planes. We have plotted the diffraction pattern in a constrained 2θ range around the strongest Bragg reflection (111) to obtain a clear increased image and shifting of peaks shown in Fig. 2. The evidence presented in this graphic demonstrates that an increase in Pd-doping from 0.5 to 5% causes the Bragg peaks to shift to the side with the higher angle. These findings lend even more credence to the conclusion that Pd ions were successfully integrated into the CeO_2 matrix [16,17].

Band Gap Shifts in Pure and Pd-doped CeO_2

The optical characteristics of the synthesized pure and Pd-doped CeO_2 nanoparticles were analysed using a UV-visible spectrophotometer. Figure 3a displays the UV-visible absorption spectra of both pure and Pd-doped CeO_2 nanoparticles. It is evident from the spectra that all samples exhibit a prominent absorption peak at approximately 390 nm. The locations of the absorption peaks for CeO_2 nanoparticles that have been Pd-doped and pure show that they have a fluorite cubic structure. The energy of the direct band gap, denoted as E_g, is determined using the Kubelka-Munk function for the purpose of determining the band gap

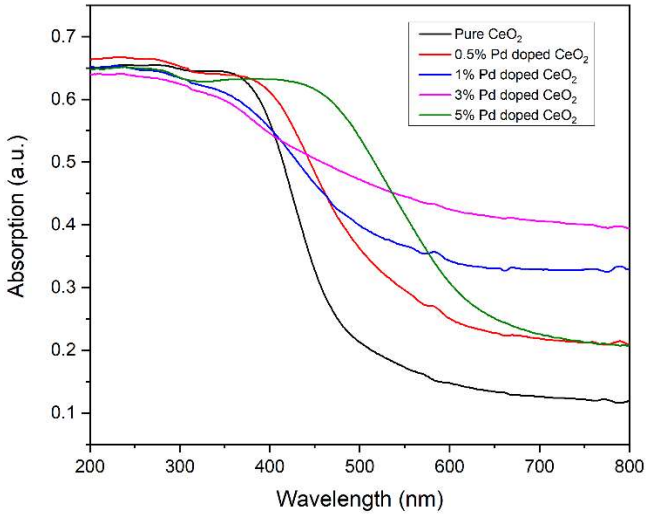

Fig. 3a. UV-visible spectra of pure and Pd-doped CeO_2.

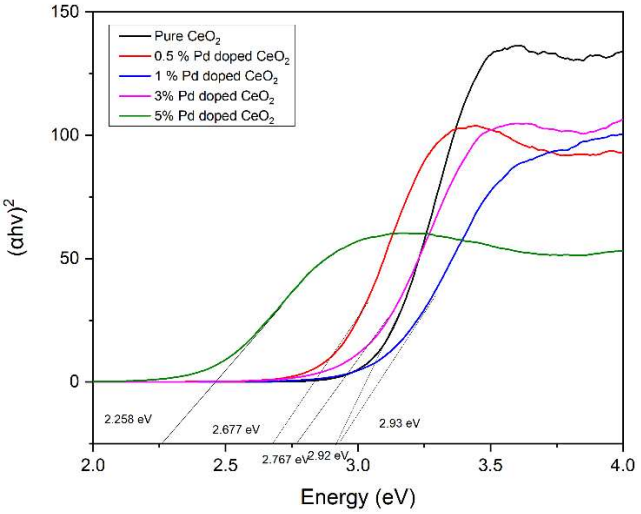

Fig. 3b. Optical bandgap energy of pure and Pd-doped CeO_2.

of the synthesized nanoparticles [18,19]. In Fig. 3b, the graph illustrates the relationship between the square of (αhv) and the corresponding energy generated. The band gap energies have been determined by projecting the linear segment of the curve onto the energy axis. The direct band gap energy, as calculated, for both pure and Pd-doped CeO_2 nanoparticles is displayed in Fig. 3b. In comparison to pure CeO_2 nanoparticles, the energy band gap (E_g) of Pd-doped CeO_2 nanoparticles has been found to have significantly moved (2.92 eV, 2.67 eV, 2.76 eV, 2.93 eV and 2.258 eV for $Pd_{0.00}Ce_{100}O_2$, $Pd_{0.5}Ce_{99.5}O_2$, $Pd_{1.0}Ce_{99.0}O_2$, $Pd_{3.0}Ce_{97}O_2$ and $Pd_{5.0}Ce_{95.0}O_2$ respectively). Keeping charge neutrality, the figures in the report depict slight modifications to the CeO_2 matrix when divalent or trivalent Pd ions replace Ce ions. This substitution process induces subtle shifts in X-ray diffraction (XRD) patterns, indicating crystal lattice modifications. These variations in peak intensity and location indicate the effective incorporation of Pd into the CeO_2 structure. These subtle structural alterations have significant effects on the material's behaviour and properties, especially in applications such as catalysis and solid-state electronics [20-21].

Raman Analysis of Pure and Pd-doped CeO_2

The synthesized nanoparticle's Raman spectra are shown in Fig. 4. Pure CeO_2 nanoparticle's Raman spectra display a noticeable peak at 464.01 cm^{-1}, which has a slight shift from the F_{2g} mode, which is the typical Raman active mode for bulk CeO_2 (459 cm^{-1}). The small particle size of this peak shift makes Vo and phonon confinement effects frequently connected with it. Additionally, it is evident from Fig. 4 that the Pd doping has systematically increased the width of this mode peak while slightly reducing the peak intensity of the F_{2g} Raman active mode [22]. These modifications, which include a shift towards a lower frequency, a drop in peak intensity, and a widening of the F_{2g} mode peak, seen in the CeO_2 Raman spectral characteristic peak, support the establishment of the crystal structures abundance of Vo defects. Based on data from XRD, SEM, and BET, the presence of Vo in these nanostructures may be due to the fact that making these nanostructures improved BETSSA. These defects (Vo) might be crucial in adjusting the physical properties (M_s and E_g) of these synthesized nanoparticles.

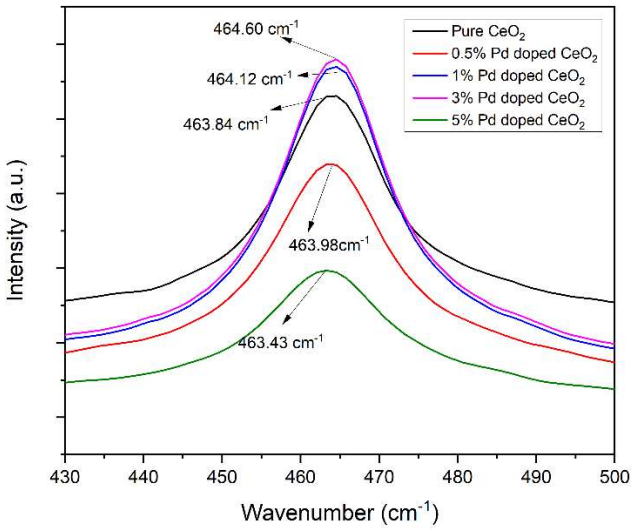

Fig. 4. Raman spectra of pure and Pd-doped CeO_2.

Paramagnetic Transition in Pure and Pd-doped CeO_2

Figure 5 illustrates the field dependence of magnetization (M-H curve) for polycrystalline samples of pure CeO_2 and $Pd_x Ce_{100-x}O_2$ (x = 0, 3, and 5.0). It is evident that pure CeO_2 exhibits the same diamagnetic behaviour as bulk samples containing Ce^{4+} ions in the $4f_0$ electronic configuration, such as CeO_2, Al_2O_3, ZnO, In_2O_3, and SnO_2. However, when 5% Pd is doped into CeO_2, a noticeable enhancement in magnetization is observed. The resulting S-shaped hysteresis loop in the 5% Pd-doped sample indicates a prevalence of magnetic states, marking a transition from diamagnetic to paramagnetic behaviour compared to pure bulk CeO_2. Surprisingly, the paramagnetic ordering appears to be suppressed as the Pd concentration increases from 3% to 5%. Nonetheless, both Pd-doped materials exhibit M-H curves that do not saturate at the maximum applied magnetic field, indicating significant magneto-crystalline anisotropy in both samples. These findings suggest a weak paramagnetic ordering in the Pd-doped samples, with 5% Pd-doped CeO_2 exhibiting a predominance of diamagnetic behaviour over paramagnetic ordering. The values of coercivity (Hc), magnetization (Ms), and retentivity (Mr) for Pd-doped CeO_2 vary depending on the doping percentage, as provided in Table 1.

Table 1. The Magnetic Properties for Pure and Pd-doped CeO_2 Nanoparticles

Magnetic properties	Pure CeO_2	3% Pd-doped CeO_2	5% Pd-doped CeO_2
Coercivity (Hc)	486.37 Oe	216.94 Oe	327.57 Oe
Field increment	500 Oe	500 Oe	500 Oe
Magnetization (Ms)	2.8342 E^{-3} emu	10.454 E^{-3} emu	3.6586 E^{-3} emu
Mass	27.000 E^{-3} g	23.3 E^{-3} g	29.7 E^{-3} g
Number of points	151	151	151
Retentivity (Mr)	1.0347 E^{-3} emu	2.2448 E^{-3} emu	1.0804 E^{-3} emu
Sensitivity	-6.7000 emu	-6.6000 emu	-6.7000 emu

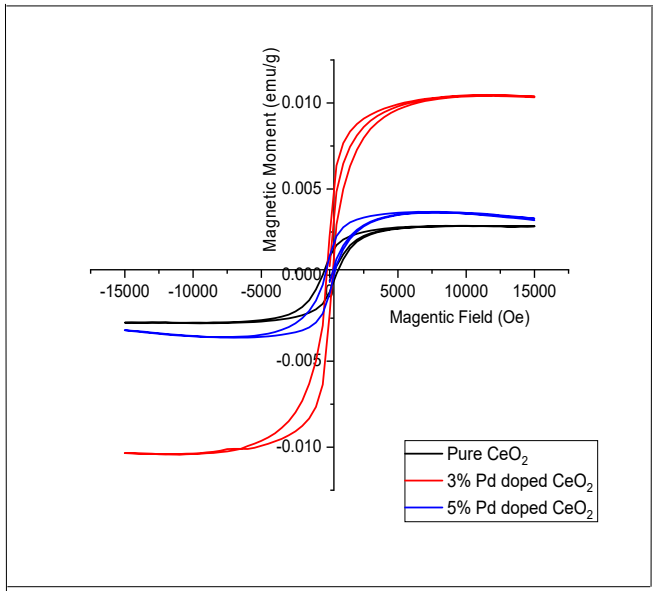

Fig. 5. Vibrating sample magnetometry spectra of pure and Pd-doped CeO_2.

SEM Imaging: Homogeneous Nanostructures of Pure and Pd-doped CeO_2

The SEM images presented in Fig. 6 clearly demonstrate that both the pure and Pd-doped CeO_2 samples possess nanostructures with zero-dimensional (0-D) morphology. The existing body of monographs consistently emphasises the high degree of homogeneity exhibited by nanoparticles, as well as their symmetrical size and spherical shape.

According to the findings depicted in Fig. 6, the particle size range of the synthesized nanoparticles (20-80 nm) has been influenced by the distinct valence states, ionic radii, and Pauling electro-negativities exhibited by the Pd and Ce cations.

Elemental Mapping and Composition Analysis of Pure and Pd-doped CeO_2

The elemental mapping of the specimens, which contained pure CeO_2 nanoparticles and CeO_2 nanoparticles doped with 3% and 5% Pd, was acquired using the EDAX spectrum, as shown in Fig. 7. The inset graph provides a visual representation of the observed distribution of Ce, Pd, and O within the sample. This graph serves as additional evidence supporting the agreement between the elemental compositions and the assessed stoichiometry. The weight and atomic percentage proportions obtainable in the tables demonstrate the elemental weight proportion percentage. The essential elemental proportions and ratios align with the anticipated elemental proportions, wherein oxygen (O), cerium (Ce), and palladium (Pd) exhibit the most prominent peaks across all samples. Figure 6 presents SEM cross-sectional images of cerium oxide nanoparticles (CeO_2 NPs) in their pure form and doped with varying concentrations of palladium (1%, 3%, and 5%). There is a documented observation that an increase in palladium concentration within cerium oxide leads to an augmented aggregation of spherical-shaped nanoparticles, characterized by a restricted range of sizes.

Insights into Chemical Bonding in Pd-doped CeO_2

XPS technology is used to examine the chemical bonding nature of Pd-doped CeO_2 NPs as shown in Fig. 8. According to the survey spectrum, the samples are made up of Ce, O,

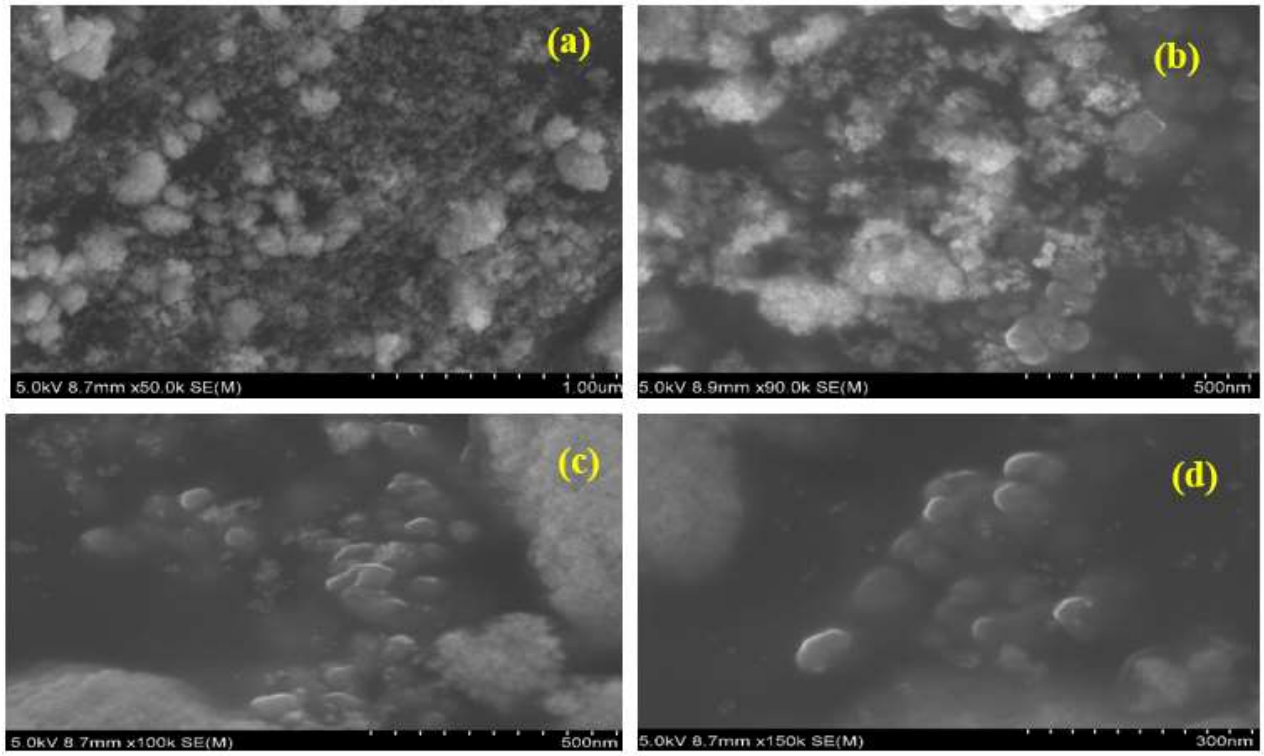

Fig. 6. SEM images of $Pd_x Ce_{100-x}O_2$ nanoparticles. (a) Pure CeO_2, (b) 1% Pd-doped CeO_2, (c) 3% Pd-doped CeO_2, (d) 5% Pd-doped CeO_2.

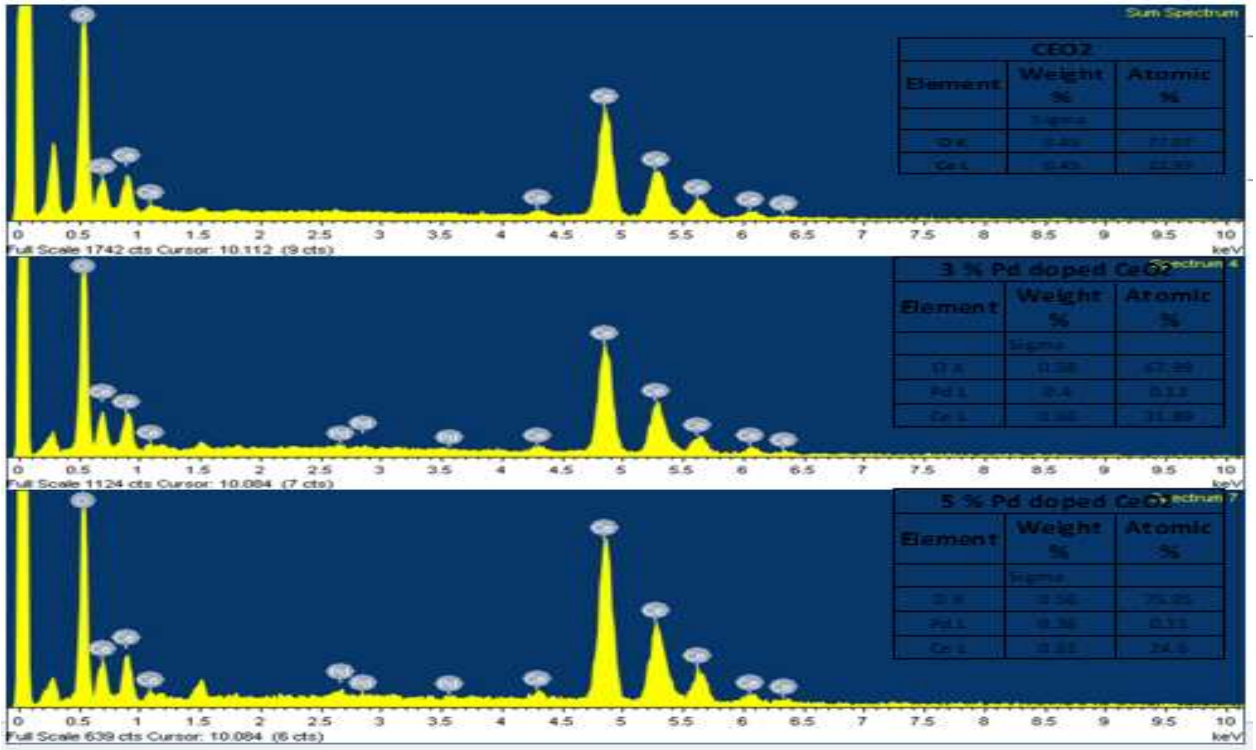

Fig. 7. The elemental mapping of pure and Pd-doped CeO_2.

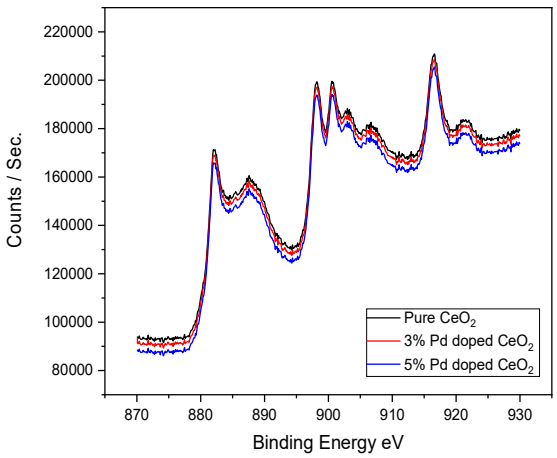

(a) Ce 3d spectra of pure and Pd-doped CeO_2

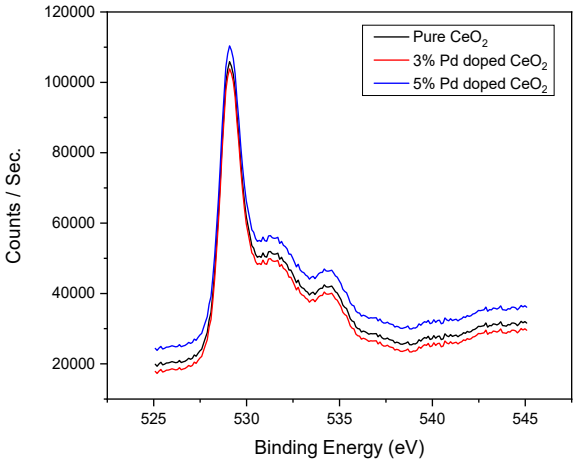

(b) O1s spectra of pure and Pd-doped CeO_2

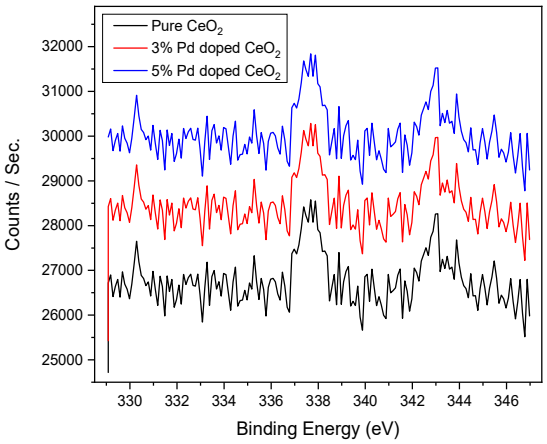

(c) Pd 3d spectra of pure and Pd-doped CeO_2

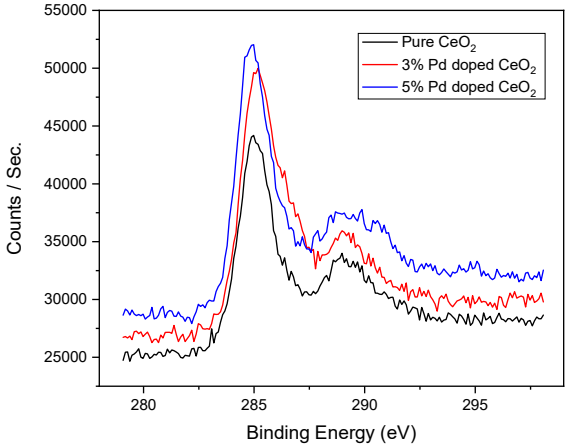

(d) C1s spectra of pure and Pd-doped CeO_2

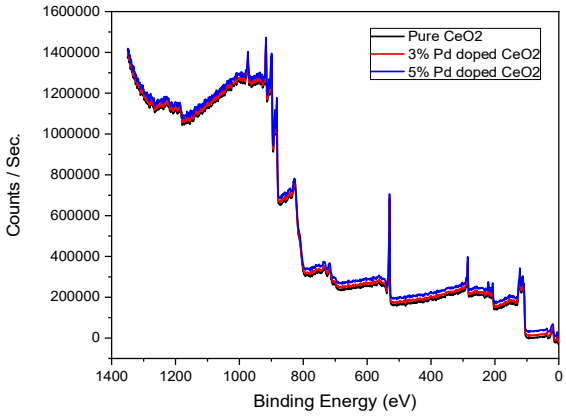

(e) XPS survey

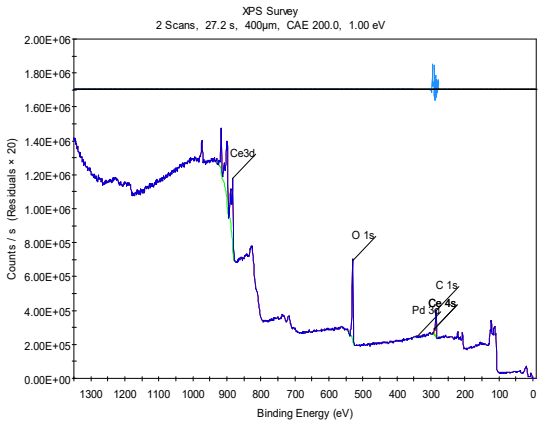

(f) XPS survey (Reference)

Fig. 8. XPS spectra of pure and Pd-doped CeO_2.

and Pd, with binding energies of 850-920 eV for Ce 3d, 530 eV for O_{1s} and 360 eV for Pd 3d respectively. Ce 3d spectra are made up of Ce $3d_{5/2}$ (882 eV) and Ce $3d_{5/2}$ (917 eV) spin-orbit doublets. The major oxidation states of CeO_2, Ce^{4+}, and Ce^{3+} are well-matched by these binding energies. The spin-orbit splitting in the Ce 3d area is well separated and is 18.6 eV [23-26]. Additionally, it is evident that Ce $3d_{5/2}$ peaks and satellite peaks (γ_1, γ_2, μ_1, and μ_2) are associated with the energy gain process. On the other hand, the Pd 3d spectra exhibit the signature of a metallic Pd peak. Metallic Pd and a well-separated 5 eV spin-orbit coupling peak at 338.2 eV (Pd $3d_{5/2}$) and 343.3 eV (Pd $3d_{5/2}$) respectively.

Moreover, the observed satellite peaks at the lower binding energy regions of Pd $3d_{5/2}$ (330.5 eV) and Pd $3d_{3/2}$(335 eV) can be attributed to the presence of Pd^+ in an oxidized state. Also, the deconvoluted O1s spectra reveal three prominent binding energies: 529.2 eV (O'''), 531.5 eV (O''), and 534.44 eV (O'). These binding energies are associated with lattice oxygen ions (Olat) and surface-adsorbed oxygen ions (Odds). The presence of oxygen vacancies resulting from the Pd ions within the crystal lattice gives rise to observable surface-adsorbed oxygen signatures, with the peak corresponding to the element C. There is evidence that the nanoparticles contain organic carbon by the binding energies observed and specifically 281.5 eV (C-C), 285.1 eV (C-O), and 288.9 eV (C-O) which shows coincidence with the reference spectrum. It is noteworthy that the Pd-doped cerium oxide nanoparticles exhibit an absence of hydroxide peaks [26-32]. The peak values of Pd-doped CeO_2 are presented in Table 2.

CONCLUSIONS

The impact of Pd-doping on polycrystalline CeO_2 nanoparticles has been investigated and synthesized via the co-precipitation method. Pd was intentionally incorporated at concentrations ranging from 0.5% to 5% into the cerium oxide lattice. Key findings and conclusions derived from this study include:

Structural Insights: Utilizing Rietveld's refinement technique on X-ray diffraction patterns, we have substantiated the presence of a fluorite-type face-centered cubic structure within the CeO_2 lattice, even after Pd doping.

Optical Transformations: Examination of UV-Vis absorption spectra has disclosed a substantial shift towards longer wavelengths, especially in the red end of the spectrum region. This shift was accompanied by a noteworthy reduction in the band gap energy as the concentration of Pd ions increased, signifying the potential for tailoring CeO_2's optical properties through controlled Pd doping.

Evidence of Doping: The variations in intensity observed in

Table 2. Peak Values for Pd-CeO_2 with Various Percentages

Name	Doping %	Peak BE	FWHM	Area (P) CPS (eV)	Atomic %
C 1s	CeO_2	284.7	2.07	490021.64	32.26
	3% Pd-CeO_2	284.9	2.16	490122.24	31.67
	5% Pd-CeO_2	285.1	2.57	490143.76	35.38
O 1s	CeO_2	530.12	3.13	171114.63	50.13
	3% Pd-CeO_2	530.14	3.84	1721414.21	51.68
	5% Pd-CeO_2	530.15	3.37	1746414.37	52.06
Ce3d5	CeO_2	882.4	3.96	6312046.97	11.85
	3% Pd-CeO_2	883.02	3.87	6335146.27	12.06
	5% Pd-CeO_2	883.09	4	6345046.11	12.45
Pd 3d	CeO_2	337.42	1.41	26525	0.11
	3% Pd-CeO_2	337.63	1.38	26905	0.11
	5% Pd-CeO_2	337.94	1.44	27605	0.11

BE: Binding Energy, CPS: Count per Second, FWHM: Full Width Half Maximum.

Raman spectra for different Pd-dopant percentages provide further confirmation of the successful incorporation of Pd into the CeO_2 lattice.

Nanoparticle Characteristics: SEM analysis has reliably confirmed that both pure CeO_2 and Pd-doped CeO_2 samples exhibit spherical-shaped nanoparticles with particle sizes ranging from approximately 20 to 80 nm.

Elemental Composition Verification: EDAX analysis has validated the elemental composition of Pd, Ce, and O, aligning with stoichiometric expectations and underlining the consistent incorporation of Pd into the CeO_2 lattice.

Chemical State Transition: XPS analysis has unveiled a change in the oxidation state of Pd ions within the Pd-doped CeO_2 samples, offering valuable insights into the chemical configurations of Pd within the lattice.

Magnetic Evolution: VSM has demonstrated a notable shift in magnetic behaviour, transitioning from diamagnetic properties in pure CeO_2 to enhanced paramagnetic characteristics with the introduction of Pd dopants. Remarkably, the optimal concentration for inducing paramagnetic behaviour was determined to be 5 mol% Pd.

These findings collectively contribute to a deeper understanding of the effects of Pd doping on CeO_2 and suggest the potential for tailoring its properties for a range of applications, including catalysis, optics, and magnetism. Continued investigation in this field offers the potential for enhancing the performance of Pd-doped CeO_2 materials within distinct technological applications.

REFERENCES

[1] Majid Darroudi, M.; Sarani, M.; Reza Kazemi, O.; Ali Khorsand, Z.; Mohammad Sadegh, Amiri., Nanoceria: Gum mediated synthesis and in vitro viability assay. *Ceram. Int.* **2014**, *40* (2), 2863-2868, DOI: 10.1016/j.ceramint.2013.10.026.

[2] Devaraja, P. B.; Avadhani, D. N.; Prashantha, S. C.; Nagabhushana, H.; Sharma, S. C.; Nagabhushana, B. M.; Nagaswarupa, H. P.; Premkumar, H. B., MgO:Eu^{3+} red nanophosphor: Low-temperature synthesis and photoluminescence properties. *Spectrochim. Acta A: Mol. Biomol. Spectrosc.* **2014**, *121*, 46-52, DOI: 10.1016/j.saa.2013.10.060.

[3] Dhananjaya, N.; Nagabhushana, H.; Nagabhushana, B. M.; Rudraswamy, B.; Sharma, S. C.; Sunitha, D. V.; Shivakumara, C.; Chakradhar, R. P. S., Effect of different fuels on structural, thermo and photoluminescent properties of Gd_2O_3 nanoparticles. *Spectrochim. Acta-A: Mol. Biomol. Spectrosc*. **2012**, *96*, 532-540, DOI: 10.1016/j.saa.2012.04.067.

[4] Wolfe, J. P.; Li, J. J., An introduction to palladium catalysis. *Tetrahedron Org. Chem. Ser.* **2007**, *26*, 1-35, DOI: 10.1016/S1460-1567(07)80050-X.

[5] Lee, Y. T.; Choi, S. Y.; Chung, Y. K., Microwave-assisted palladium-catalyzed regioselective cyanothiolation of alkynes with thiocyanates. *Tetrahedron Lett.* **2007**, *48* (32), 5673-5677, DOI: 10.1016/j.tetlet.2007.06.041.

[6] Mohanraj, K.; Balasubramanian, D.; Porkumaran, K.; Jhansi, N.; Chandrasekaran, J., Impact of Ce content on cubic phase cerium–cadmium oxide (Ce–CdO) nanoparticles and its n-CeCdO/p-Si junction diodes. *J. Mater. Sci.: Mater. Electron*. **2018**, *29*, 20439-20454, DOI: 10.1007/s10854-018-0178-7.

[7] Begines, B.; Ortiz, T.; Pérez-Aranda, M.; Martínez, G.; Merinero, M.; Argüelles-Arias, F.; Alcudia, A., Polymeric Nanoparticles for Drug Delivery: Recent Developments and Future Prospects. *Nanomaterials (Basel)*. **2020**, *10* (7), 1403, DOI: 10.3390/nano10071403.

[8] Păduraru, D. N.; Ion, D.; Niculescu, A. G.; Mușat, F.; Andronic, O.; Grumezescu, A. M.; Bolocan, A., Recent Developments in Metallic Nanomaterials for Cancer Therapy, Diagnosing and Imaging Applications. *Pharmaceutics*. **2022**, *14* (2), 435, DOI: 10.3390/pharmaceutics14020435.

[9] Chang, J. H.; Kumar, M.; Nayak, A. K., Nanostructured materials for photoelectrochemical water splitting. IOP Publishing, **2021**, p. 1-20, DOI: 10.1088/978-0-7503-3699-4.

[10] Itamar, W.; Ruben, M.; Daphna, M.; Heinz, D.; Gisela, D.; Klaus, Z., Photosensitized reduction of carbon dioxide to methane and hydrogen evolution in the presence of ruthenium and osmium colloids: strategies to design selectivity of products distribution. *J. Am. Chem. Soc.* **1987**, *109*, 6080-6086, DOI: 10.1021/ja00254a029.

[11] Desai, N., Challenges in development of nanoparticle-

based therapeutics. *AAPS J*. **2012**, *14* (2), 282-95, DOI: 10.1208/s12248-012-9339-4.

[12] Qin, Y. H.; Yang, H. H.; Zhang, X. S.; Li, P.; Ma, C. A., Effect of carbon nanofibers microstructure on electrocatalytic activities of Pd electrocatalysts for ethanol oxidation in alkaline medium. *Int. J. Hydrog. Energy*. **2010**, *35* (15), 7667-7674, DOI: 10.1016/j.ijhydene.2010.05.034.

[13] Zhang, Z.; Liu, J.; Gu, J.; Su, L.; Cheng, L., An overview of metal oxide materials as electrocatalysts and supports for polymer electrolyte fuel cells. *Energy Environ. Sci*. **2014**, *7* (8), 2535-2558, DOI: 10.1039/C3EE43886D.

[14] Abdulridha, A. A.; Allah, M. A. A. H.; Makki, S. Q.; Sert, Y.; Salman, H. E.; Balakit, A. A., Corrosion inhibition of carbon steel in 1 M H_2SO_4 using new Azo Schiff compound: Electrochemical, gravimetric, adsorption, surface and DFT studies. *J. Mol. Liq.* **2020**, *315*, 113690, DOI: 10.1016/j.molliq.2020.113690.

[15] Tigabu Bekele, M., Synthesis and characterization of CdS/CeO_2 Nanocomposite with improved visible-light photocatalytic degradation of methyl orange dye. *J. Plant Sci. Phytopathol.* **2022**, *6*, 65-74, DOI: 10.29328/journal.jpsp.1001077.

[16] Kumaran, C.; Baskaran, I.; Vanmathi Selvi, K.; Senthamil Selvi, C.; Rajkumar, P.; Selvaraj, S., Antimicrobial activity of Cobalt doped Cerium Oxide (Co-CeO2) nanoparticles against selected food pathogens. *Inter. Res. J. Multi Tech.* **2023**, *5* (4), DOI: 10.54392/irjmt2344.

[17] Kumaran, C.; Baskaran, I.; Sathyaseelan, B.; Senthilnathan, K.; Manikandan, E.; Sambasivam, S., Effect of doping of iron on structural, optical and magnetic properties of CeO_2 nanoparticles. *Chem. Phys. Lett*. **2022**, 808, 140110, DOI: 10.1016/j.cplett.2022.140110.

[18] Sherly, E. D.; Judith Vijaya, J.; John Kennedy, L., Effect of CeO_2 coupling on the structural, optical and photocatalytic properties of ZnO nanoparticle. *J. Mol. Struct.* **2015**, *1099*, 114-125, DOI: 10.1016/j.molstruc.2015.05.057.

[19] Jih-Hsing, C.; Ashalata, P.; Cheng-Di, D.; Shan-Yi, S.; Narendhar, C.; Mohanraj, K., Synthesis of Pd-Fe_2O_3 nanoflakes nanocomposite for superior energy storage device. *J. Tai. Inst. Chemi. Eng.* **2022**, *140*, 104562, DOI: 10.1016/j.jtice.2022.104562.

[20] Truffault, L.; Minh-Tri, T.; Thierry, D.; Konstantin, K.; Valérie, H.; Cyriaque, S.; Caroline, A.; Nevirkovets, I. P.; Alain, P.; Olivier, V.; Blondeau, J. P., Application of nanostructured Ca doped CeO_2 for ultraviolet filtration. *Mater. Res. Bull.* **2010**, *45* (5), 527-535, DOI: 10.1016/j.materresbull.2010.02.008.

[21] Ravishankar, T. N.; Ramakrishnappa, T.; Nagaraju, G.; Rajanaika, H., Synthesis and Characterization of CeO_2 Nanoparticles via Solution Combustion Method for Photocatalytic and Antibacterial Activity Studies. *Chem. Open*. **2015**, *4* (2), 146-54, DOI: 10.1002/open.201402046.

[22] Weber, W. H.; Hass, K. C.; McBride, J. R., Raman study of CeO_2: Second-order scattering, lattice dynamics, and particle-size effects. *Phys. Rev. B Condens Matter*. **1993**, *48* (1), 178-185, DOI: 10.1103/physrevb.48.178.

[23] Rema Devi, B. S.; Raveendran, R.; Vaidyan, A. V., Synthesis and characterization of Mn^{2+}-doped ZnS nanoparticles. *Pramana-J. Phys.* **2007**, *68* (4), 679-687, DOI: 10.1007/s12043-007-0068-7.

[24] Feng, Z.; Siu-Wai, C.; Jonathan, E. S.; Ebru, A.; Qiang, J.; Richard, D. R.; Irving, P. H., Cerium oxide nanoparticles: Size-selective formation and structure analysis. *Appl. Phys. Lett.* **2002**, *80* (1), 127-129, DOI: 10.1063/1.1430502.

[25] Preisler, E. J.; Marsh, O. J.; Beach, R. A.; McGill, T. C., Stability of cerium oxide on silicon studied by x-ray photoelectron spectroscopy. *J. Vac. Sci. Technol. B*. **2001**, *19* (4), 1611. DOI: 10.1116/1.1387464.

[26] Fernandes, V.; Graff, I. L.; Varald, J.; Amaral, L.; Fichtner, P.; Demaille, D.; Zheng, Y.; Schreiner, W. H.; Mosca, D. H., Valence Evaluation of Cerium in Nanocrystalline CeO_2 Films Electrodeposited on Si Substrates. *J. Electrochem. Soc.* **2012**, *159* (1), K27, DOI: 10.1149/2.056201jes.

[27] Henderson, M. A.; Perkins, C. L.; Engelhard, M. H.; Thevuthasan, S.; Peden, C. H. F., Redox properties of water on the oxidized and reduced surfaces of CeO_2 (111). *Surf. Sci.* **2003**, *526* (1-2), 1-18, DOI: 10.1016/S0039-6028(02)02657-2.

[28] Hugenschmidt, M. B.; Gamble, L.; Campbell, C. T., The interaction of H_2O with a TiO_2(110). *Surf. Sci.* **1994**, *302* (3), 329-340, DOI: 10.1016/0039-6028(94)90837-0.

[29] Lykhach, Y.; Johanek, V.; Aleksandrov, H. A.; Kozlov, S. M.; Happel, M.; Skala, T.; Petkov, P. S.; Tsud, N.; Vayssilov, G. N.; Prince, K. C.; Neyman, K. M., Water chemistry on model ceria and Pt/ceria catalysts. *J. Phys. Chem. C.* **2012**, *116* (22), 12103-12113, DOI: 10.1021/jp302229x.

[30] Nikolova, M. P.; Chavali, M. S., Metal Oxide Nanoparticles as Biomedical Materials. *Biomimetics*. **2020**, *5* (2) 27, DOI: 10.3390/biomimetics5020027.

[31] Malathi, S.; Jagathy, K.; Ram Kumar, A.; Selvaraj, S., An *in-vivo* synergistic research on the assessment of the phytocompound capped silver nanoparticles from Raphanus sativus leaf extract and curcuma longa against UTI-causing E. coli. *Phys. Chem. Res.* **2022**, *10* (4), 581-588, DOI: 10.22036/PCR.2022.326373.2021.

[32] Mani, M.; Okla, M. K.; Selvaraj, S.; Kumar, A. R.; Kumaresan, S.; Muthukumaran, A.; Kaviyarasu, K.; El-Tayeb, M. A.; Elbadawi, Y. B.; Almaary, K. S.; Almunqedhi, B. M. A., A novel biogenic Allium cepa leaf mediated silver nanoparticles for antimicrobial, antioxidant, and anticancer effects on MCF-7 cell line. *Environ. Res.* **2021**, *198*, 11199, DOI: 10.1016/j.envres.2021.111199.